

Synthesis of Nitrogen-Rich Carbon Nitride-Based Hybrids and a New Insight of Their Battery Behaviors

Jang Mee Lee,^{*[a]} Stalin Joseph,^[a] Ian Chirchir Bargoria,^[a] Sungho Kim,^[a, b] Gurwinder Singh,^[a] Jae-Hun Yang,^[a] Kavitha Ramadass,^[a] Rohan Bahadur,^[a] Xiaojiang Yu,^[c] Mark BH Breese,^[c, d] Jiabao Yi,^[a] and Ajayan Vinu^{*[a]}

N-rich carbon nitride (CN) is a promising framework that can generate innovative hybrid structures for energy applications. However, the low thermal stability of N atoms in the CN matrix is a major drawback as the crystallization of the hybridized counterpart requires a high temperature. Herein, we report the successful synthesis of the hybrid of N-rich CN and Fe_{1-x}S at 700°C by constructing a stable C–N–Fe–S heterointerface using a Fe-incorporated metal-organic framework (MOF) and dithioxamide containing C, N and S atoms. The hybrids display

promising capacities toward Li⁺ and Na⁺ ions storage, highlighting the beneficial role of N-rich CN on battery performance. By systematically investigating their structure and electrochemical properties, we show that N-rich CN, along with the heterointerface, not only acts as a hybridization matrix that helps facilitate the charge transfer kinetics but also generates substantial capacity. This unique study reveals a powerful platform for the rational design of N-rich CN based hybrids from MOF.

As an alternative to the graphite in lithium-ion batteries (LIBs), carbon nitride (CN) has shown a high promise with a theoretical capacity of 524 mAhg⁻¹ that is ~1.5 times larger than graphite.^[1] In such systems, the localized electrons adjacent to N atoms along with lone pair electrons act as active sites, which not only facilitate the adsorption of alkali metal ions but also enable a facile hybridization with foreign species.^[2] Since the topological structure of the CN greatly affects its physicochemical and electronic properties, researches to vary the C/N stoichiometric ratio have been widely conducted toward various applications.^[3] Taking the pivotal role of N atoms into consideration, our group explored N-rich CNs beyond a conventional stoichiometry of C₃N₄ in order to improve the battery functionalities of the CN-based systems.^[4] It was demonstrated that the N-richness in CN induced a favorable adsorption energy toward Li⁺ and Na⁺ ions via

density functional theory calculations and indeed enhanced battery functionalities.^[4] Accordingly, in addition to the role of a hybridization matrix, it is highly anticipated that the N-rich CN itself can contribute to the battery capacity, which outweighs the performance of a typical C₃N₄. Also, a chronic issue of low electrical conductivity exacerbated by N-richness can be mitigated by constructing an intimate heterointerface (HI) with the hybridized components, which promotes charge transfer kinetics.^[5] However, owing to the low thermal stability of N atoms, the N-rich CNs are synthesized mainly under mild temperatures below 500°C,^[6] which is insufficient to highly crystallize the hybridized counterpart such as metal sulfides at the same time. Therefore, it is critical to address how to design N-rich CN based hybrids.

In this investigation, we propose a simple method to overcome this challenge by mixing the Fe-MIL-100 structure (C₁₈H₈Fe₃O₁₆) with the stable covalent bonding even under a high temperature of 700°C^[7] with dithioxamide (DTO, C₂H₄N₂S₂) via in-situ chemical transition. As the DTO contains C, N and S atoms, an iron sulfide can be formed simultaneously with the N-rich CN via a C–N–Fe–S HI (CNF, Figure 1A). Two different materials were prepared by varying the molar ratio of DTO and Fe-MIL-100 of 1:0.045 and 1:0.18, denoted as CNF1 and CNF2, respectively. These intriguing hybrids deliver promising capacities of ~1750 mAhg⁻¹ and ~300 mAhg⁻¹ in LIB and sodium-ion battery (SIB) at 0.1 Ag⁻¹, respectively, which are the highest ever value reported for N-rich CNs. Furthermore, we conducted systematic characterization of the electrochemical behavior toward Li⁺ and Na⁺ storages and demonstrated the roles of N-rich CN, iron sulfide and their HI in hybrids which significantly contribute to the battery functionality.

Details of the experimental procedure and characterization are described in Supporting Information. Formation of a

[a] Dr. J. Mee Lee, Dr. S. Joseph, I. Chirchir Bargoria, Dr. S. Kim, Dr. G. Singh, J.-H. Yang, Dr. K. Ramadass, R. Bahadur, Prof. J. Yi, Prof. A. Vinu
Global Innovative Center for Advanced Nanomaterials (GICAN), School of Engineering
College of Engineering, Science and Environment
The University of Newcastle,
Callaghan, NSW 2308, Australia
E-mail: Jangmee.lee@newcastle.edu.au
Ajayan.vinu@newcastle.edu.au

[b] Dr. S. Kim
GIST Central Research Facilities
Gwangju Institute of Science and Technology (GIST)
Gwangju, 61005, Republic of Korea

[c] Dr. X. Yu, Dr. M. BH Breese
Singapore Synchrotron Light Source, National University of Singapore
Singapore 117603

[d] Dr. M. BH Breese
Department of Physics
National University of Singapore
Singapore, 117542

 Supporting information for this article is available on the WWW under
<https://doi.org/10.1002/batt.202100369>

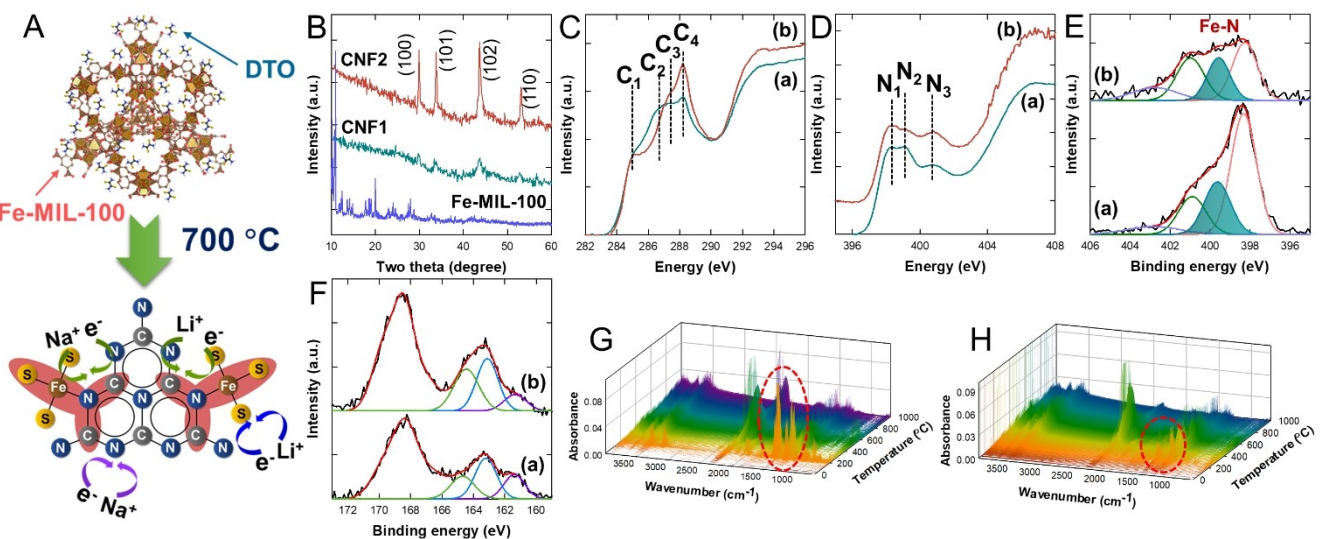


Figure 1. A) Schematic illustration of CNF hybrid. B) Powder XRD patterns of Fe-MIL-100 (blue), CNF1 (cyan) and CNF2 (red). NEXAFS spectra of C) C K-edge and D) N K-edge and XPS spectra of E) N 1s and F) S 2p for a) CNF1 and b) CNF2. TG-FTIR results of G) DTO precursor and (H) mixed DTO and Fe-MIL-100

pyrrhotite Fe_{1-x}S from Fe-MIL-100 upon hybridization with DTO is confirmed by X-ray diffraction (XRD, Figure 1B).^[8] To investigate local chemical environment that constitutes CNFs, analyses of near edge X-ray absorption fine structure (NEXAFS) and X-ray photoelectron spectroscopy (XPS) were carried out. According to C K-edge NEXAFS, four different characteristic features (peaks $\text{C}_1\text{--}\text{C}_4$) are detected at 285, 286.5, 287.3 and 288.3 eV (Figure 1C), which correspond to $\text{C} 1s \rightarrow \pi^*$ transitions of $\text{C}=\text{C}$, $\text{C}-\text{NH}-\text{C}/\text{C}-\text{S}$, $\text{C}=\text{N}$ and aromatic $\text{C}-\text{N}-\text{C}$ bonding, respectively. The local structure around C atoms appears to vary mainly in the peaks C_2 and C_4 between CNF1 and CNF2. Obviously, the peak C_4 becomes more intense at CNF2 and is ascribed to the expanded aromatic $\text{C}-\text{N}-\text{C}$ bonding that constitutes CN framework. Inversely, the $\text{C}-\text{NH}-\text{C}$ bonding (peak C_2) decreases at CNF2, which coincides well with the formation of a highly conjugated organic template. In the N K-edge NEXAFS (Figure 1D), three peaks of N_1 , N_2 and N_3 are observed at 398.5, 399.1 and 401.3 eV for both CNF hybrids which correspond to the $\text{N} 1s \rightarrow \pi^*$ transitions of aromatic $\text{C}-\text{N}-\text{C}$ (pyridinic-like N), $\text{N}-\text{C}=\text{N}$ and graphitic N, respectively.^[9]

Deconvoluted N 1s XPS spectra cross-confirmed the higher conjugation of the CN at CNF2 rather than CNF1 as the portion of graphitic N at 400.9 eV noticeably increases in the whole integrated area (Figure 1E). Interestingly, the peak of $\text{Fe}-\text{N}$ bonding is observed at 399.4 eV, revealing that the HI of CNF hybrids is coupled between the CN and Fe_{1-x}S based on $\text{Fe}-\text{N}$ bonding.^[7,10] Two peaks at 398.4 and \sim 403 eV represent pyridinic N and oxidized pyridinic N, respectively.^[11] The Fe L_{3,2}-edge NEXAFS spectra of CNF hybrids confirm the coexistence of Fe^{2+} and Fe^{3+} ions (Figure S1).^[12] In S 2p XPS spectra (Figure 1F), the peaks at 161.4, 163.1 and 164.3 eV are from the bonding features of $\text{C}-\text{S}$, $\text{Fe}-\text{S}$ and $\text{C}=\text{S}$, respectively, indicating incorporation of S atoms on the CN as well as on Fe_{1-x}S . The additional peaks at over 166 eV are related to sulfate-chemical environments. As shown in chemical compositions by CHNS

and inductively coupled plasma (ICP) analyses (Table 1), CNF hybrids exhibit higher stoichiometric ratios of C and N atoms than a typical C_3N_4 .

In comparison to S-doped CN from only a DTO precursor ($\text{C}_3\text{N}_{1.32}\text{S}_{0.05}$),^[13] the CNFs show strikingly higher content of N and S atoms, suggesting that these two elements are remarkably thermo-stabilized via hybridization. This could be due to the $\text{Fe}-\text{N}$ coupling, largely established in a HI of the hybrids. Thermogravimetric-Fourier transform infrared spectroscopy (TG-FTIR) analyses clearly confirm less N and S atoms being released as NO_2 and SO_2 gases at \sim 1600 and \sim 1350 cm^{-1} , respectively, during synthetic processing of CNF hybrids. This suggests a higher thermal stability of N and S atoms rather than an unhybridized reactant (Figures 1G–H and S2–S3).

Distribution of composed atoms is confirmed by elemental-mappings (Figure 2A). For a nanosheet (NS)-like morphology (marked by an arrow), C and N atoms are largely distributed while S and Fe atoms are less evenly spread, hence, underscoring polymerization of the CN as a form of NSs, as previously reported.^[14] According to high resolution transmission electron microscopy (HRTEM), it appears that the particles are integrated onto the CN (Figure 2B) and the lattice fringes show interplanar distance of 0.29 nm, which corresponds to the (100) plane of hexagonal Fe_{1-x}S crystals (Figures 2C and 1B). Furthermore, through field emission scanning electron microscopy (FESEM), the CNF1 appears to possess large number of the CN NSs with small Fe_{1-x}S particles while highly aggregated Fe_{1-x}S particles

Table 1. Chemical compositions of CNF hybrid structures.

Sample	Carbon [at%]	Nitrogen [at%]	Sulfur [at%]	Chemical composition
CNF1	38.98	64.68	8.38	$\text{Fe}_{0.18}\text{C}_{3.49}\text{N}_{0.64}\text{S}_{0.05}$
CNF2	27.03	39.94	18.78	$\text{Fe}_{0.72}\text{C}_{3.44}\text{N}_{0.28}\text{S}_{0.05}$

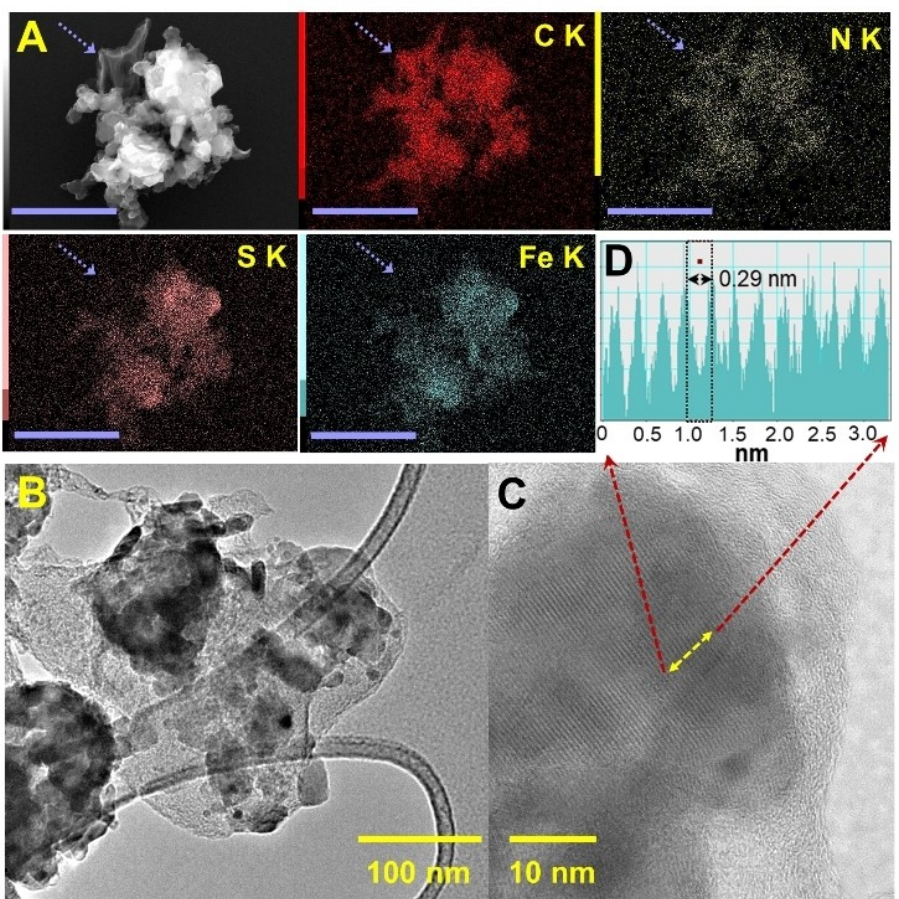


Figure 2. A) Elemental-mappings, B and C) HR-TEM images of CNF hybrid and D) the line profile of the corresponding HR-TEM image. In elemental-mappings, the scale bar represents 2 μm .

are quite dominant for the **CNF2** rather than the CN NSs, which corresponds well to the XRD and CHNS results (Figure S4).

The LIB performances of the CNF materials were conducted by measuring the cycling behavior at 0.1 and 1 A g^{-1} (Figures 3A and 3B). Both hybrids deliver an initial Coulombic efficiency (CE) of 70%–75% due to the formation of the surface electrolyte interface (SEI) layer (Figure S5A). Under a slow current density of 0.1 A g^{-1} , the specific capacity of **CNF2** with larger Fe_{1-x}S content appears to gradually increase for 200 cycles, reaching $\sim 1750 \text{ mAh g}^{-1}$ whereas the specific capacity of **CNF1** is quite constant over 200 cycles (Figure 3A). This observation corresponds to a variation in electrochemical impedance spectroscopy (EIS) measurements before and after battery cycling. A semicircle for **CNF2** appears to be remarkably reduced upon LIB cycling, indicating a reduction in charge transfer resistance whereas that for **CNF1** is quite similar even upon cycling (Figure S6). Solution resistance (R_{sol}), SEI resistance (R_{SEI}) and charge transfer resistance (R_{CT}) are quantified through simulations using an equivalent circuit (Figure S7 and Table S3). After battery cycling, the R_{CT} value of **CNF2** hybrid is estimated to be 5.82Ω , which is remarkably reduced as compared with the same cell before cycling (221Ω for R_{CT}). On the other hand, the **CNF1** possesses quite similar R_{CT} values even after cycling, which is consistent with the cycling behavior. Also, at a fast

current density of 1.0 A g^{-1} , **CNF2** appears to be more active in LIB performance after 200 cycles rather than **CNF1** (Figure 3B). The subsequent rate capability highlights the superior performance of **CNF2** across a wide range of current densities by delivering $1480, 1381, 1260, 1012, 792, 526$ and 391 mAh g^{-1} at 0.05 – 3.0 A g^{-1} .

In SIB, in stark contrast to the LIB, **CNF1** delivers the specific capacity of $\sim 300 \text{ mAh g}^{-1}$ after 100 cycles at 0.1 A g^{-1} , which outweighs the performance of **CNF2** (Figures 3D and S5B). According to the EIS measurement, a negligible difference is observed for the **CNF1** after SIB cycling whereas the cycled-**CNF2** appears two semicircles, which could be due to the emergence of other phase during cycling (Figure S8). Based on the simulations with equivalent circuit (Figure S9), R_{CT} value for the cycled-**CNF1** is estimated to be similar with the same cell before cycling (331Ω and 340Ω for before and after cycling, Table S4). For the cycled-**CNF2**, we could simulate the EIS data with two different R_{CT} components (290Ω for $R_{\text{CT}1}$ and 282Ω for $R_{\text{CT}2}$) upon SIB cycling, which infers existence of two different phases. The subsequent rate capability stresses the superior performance of **CNF1**, which exhibits $322, 289, 256, 169$ and 95 mAh g^{-1} at 0.05 – 1.0 A g^{-1} . As compared to the relevant literatures (Figures 3C and 3E and Tables S1–S2), the LIB performance of the **CNF2** hybrid is the best while the **CNF1**

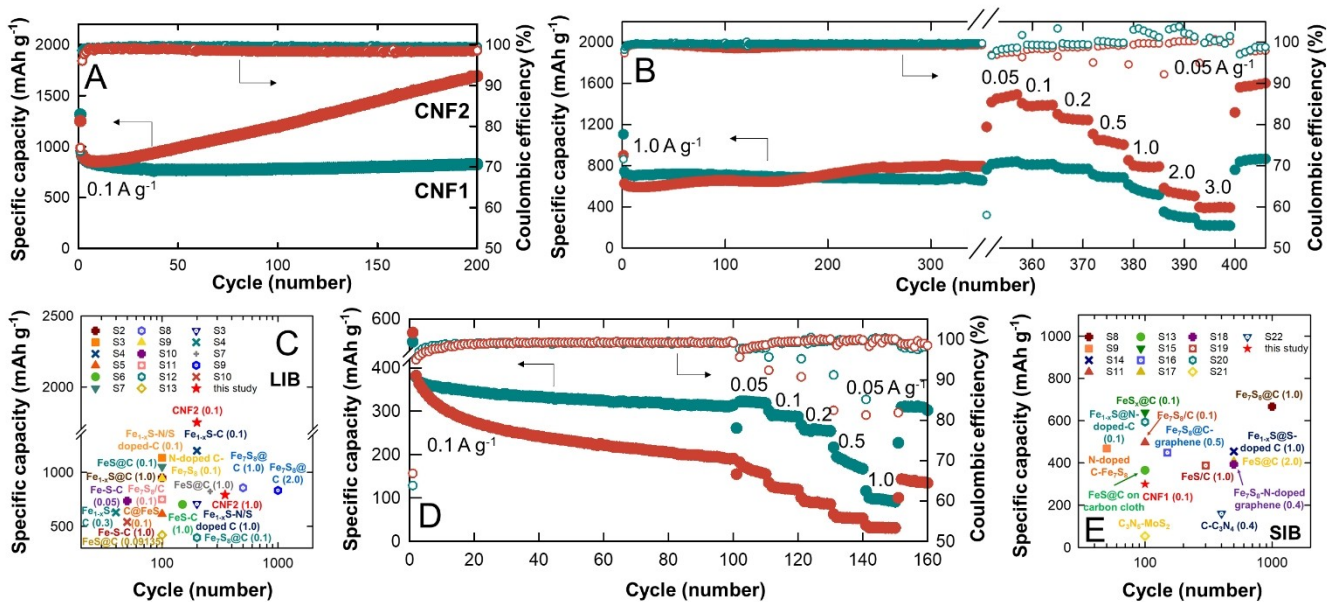


Figure 3. Li⁺ storage performances at A) 0.1 A g⁻¹ and B) 1.0 A g⁻¹ and subsequent rate capability of CNF1 (cyan) and CNF2 (red) at 0.05–3.0 A g⁻¹. D) Na⁺ storage performance at 0.1 A g⁻¹ and subsequent rate capability of CNF1 (cyan) and CNF2 (red) at 0.05–1.0 A g⁻¹. Comparisons of C) LIB and E) SIB performances of CNF with the relevant literatures. In the comparison, the value in a round bracket indicates the current density (A g⁻¹) for the battery performance.

delivers somewhat lower SIB capacity rather than the other iron sulfide-based hybrids. However, taking a dominant N-rich CN species in the CNF1 hybrid into account, the SIB performance of CNF1 outweighs that of the CN-based materials.

To figure out not only the origin of the battery behavior of CNFs in LIB and SIB but also the critical factors affecting the performance, cyclic voltammetry (CV) analyses and ex-situ XRD were carried out with a comparison before and after cycling. The as-prepared battery cells with CNFs show a cathodic peak at 1.40 V and anodic peak at 1.89 V, which is an indicator for a conversion reaction of Fe_{1-x}S (Figures 4A and 4B).^[15] This underscores the prominent role of Fe_{1-x}S phases responsible for Li⁺ ion storage at the early stage of LIB cycling. In addition, there is a negligible but distinct hump in the anodic range of 1.0–1.5 V and many papers define these peaks as intermediate steps of Li₂FeS₂ formation.^[16] The broad CV peak seems very minor in the initial stage whereas the conversion reaction of Fe_{1-x}S appears to be dominant. However, interestingly, those broad peaks of CNF1 become significantly pronounced upon LIB cycling while the peaks of conversion reaction become negligible (Figure 4A). To understand the phenomenon, ex-situ XRD after cycling was performed. The cell for ex-situ XRD was suspended at the charging stage. The peaks at ~23° and 44° are observed for CNF1 which are indexed as elemental sulfur and iron metal, respectively, inferring that the markedly depressed Fe_{1-x}S-derived conversion reaction for cycled CNF1 could be due to the phase separation (Figure 4E).^[17] Hence, for CNF1, the peaks at 1.0–1.5 V are assumed to be related to Li⁺ storage on a CN or at a HI, not the intermediate steps of the conversion reaction on Fe_{1-x}S.^[18] Also, via the FESEM, we confirm that the CNF1 maintains its NS morphology even after LIB

cycling, which well retains the CN contents without any collapse (Figure S10).

On the contrary, CNF2 shows quite similar CV curves which still maintain the conversion reaction peaks even after the cycling, implying a constant infusion of Fe_{1-x}S-derived conversion reactions on the battery capability of CNF2 (Figure 4B). Also, the peaks related to elemental sulfur or iron metal are absent in ex-situ XRD of CNF2, underscoring no collapse of Fe_{1-x}S phases (Figure 4E). As different from CNF1, the anodic peak at 1.4 V and cathodic peak at 0.85 V for CNF2 can be interpreted as an intermediate step for the conversion reaction of Fe_{1-x}S.

CV curves in the SIB exhibit obvious redox couples (cathodic peaks at ~0.9 V and ~0.25 V and anodic peaks at ~1.4 V and ~1.85 V) for both CNF hybrids. This is well-known for the conversion reaction of Fe_{1-x}S toward Na⁺ storage (Figures 4C and 4D).^[8,19] The redox peaks associated with the CN seem to be blurred because their positions overlap with Fe_{1-x}S-derived peaks. Upon SIB cycling, CNF2 appears to have a quite different CV shape with depressed redox peaks of conversion reaction while CNF1 maintains its original CV curve. Through ex-situ XRD (Figure 4F), it is found that a Fe₂O₃ phase appears in the CNF2 upon SIB cycling, which corresponds to a characteristic anodic peak of Fe₂O₃ appeared at ~1.75 V in the CV (Figure 4D).^[20]

To summarize the observations, the CNF hybrids appear an obvious difference in the electrochemical behaviors between the LIB and SIB. In the LIB system, the CNF2 with larger Fe_{1-x}S phase displays an obvious increasing capacity with the cycle number, which would be delivered based on a conversion reaction by Fe_{1-x}S species. This can be explained as

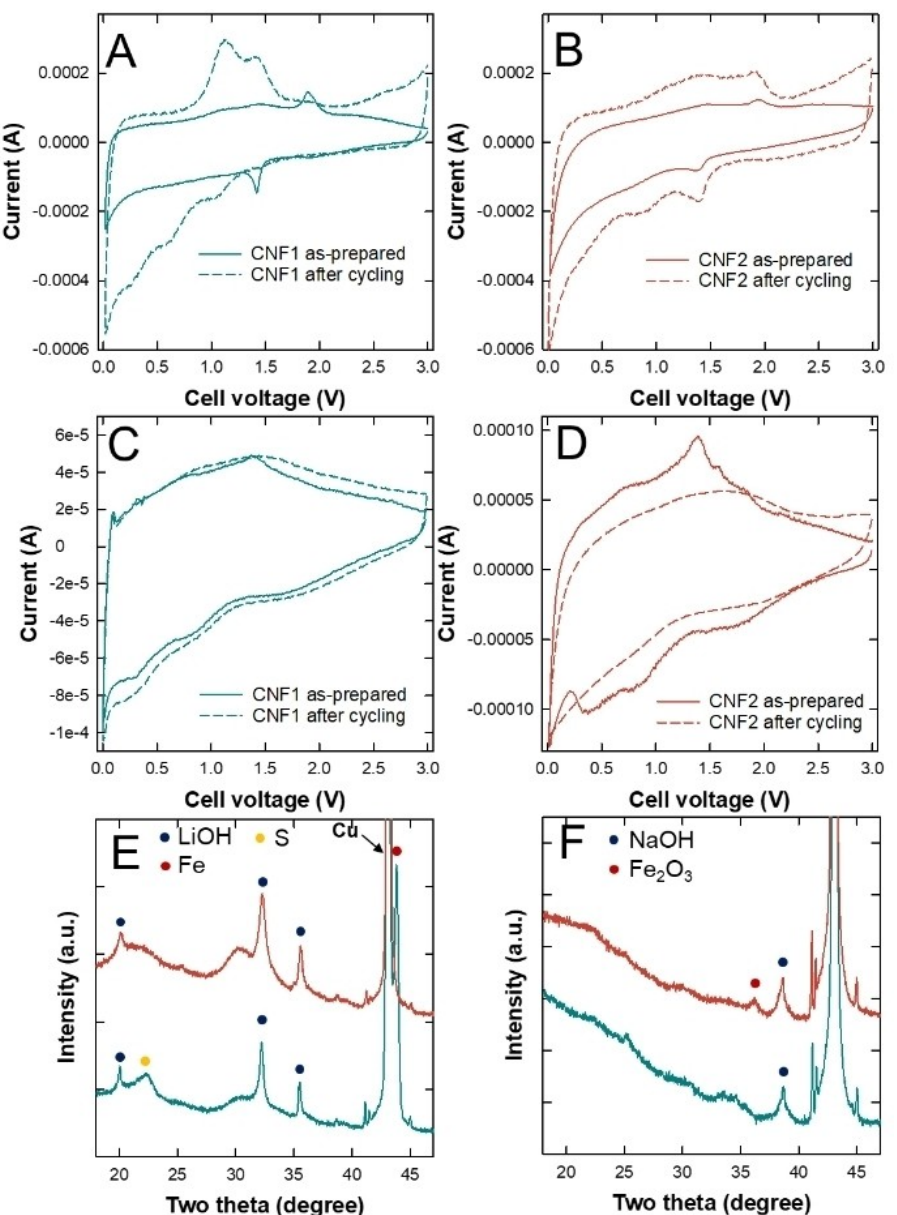


Figure 4. CV curves of the A, C) CNF1 and B, D) CNF2 with a comparison before and after battery cycling toward A, B) Li⁺ and C, D) Na⁺ storages. Ex-situ XRD of CNF1 (cyan) and CNF2 (red) upon E) LIB and F) SIB cycling.

an extended surface area and shortened Li⁺ ion diffusion path for efficient interfacial redox reaction.^[21] In such cases, it is well known that the CN acts as a hybridization matrix to support the conversion reaction, which prevents an agglomeration and boosts a reversibility. Considering the strong Fe–N coordination at the HI of the CNF2 hybrid, the N-rich CN species would provide sufficient active sites for efficient hybridization with Fe_{1-x}S species by supplying a plenty of N atoms on the surface. On the contrary, the CNF1 shows high consistency in its specific capacity notwithstanding a Fe_{1-x}S phase separation into Fe metal and elemental sulfur, inferring a negligible effect of Fe_{1-x}S phase on the electrochemical behavior of CNF1 hybrid. Apart from this, the maintenance of NS morphology for the cycled-CNF1 stresses a significant effect of the N-rich CN species on

the specific capacity hybrid rather than Fe_{1-x}S. Taking the CV variation during battery cycling into account, we believe that the N-rich CN with a HI significantly affects the battery performance. Considering a negligible contribution of Fe_{1-x}S phase-based conversion reaction, the specific capacity of 820 mAh g⁻¹ for CNF1 after 200 cycles is quite a promising value in LIB. It should be noted that we do not claim the total contribution of N-rich CN on generating a capacity of 820 mAh g⁻¹ for CNF1 hybrid but there could be a synergistic effect of the N-rich CN and established C–N–Fe–S HI on the capacity other than the conversion reaction. In SIB system, the Fe_{1-x}S-derived conversion reaction seems to be dominant for both of CNF hybrids based on the CV curves. Due to the severe pulverization effect from large size of Na⁺ ions, the morphol-

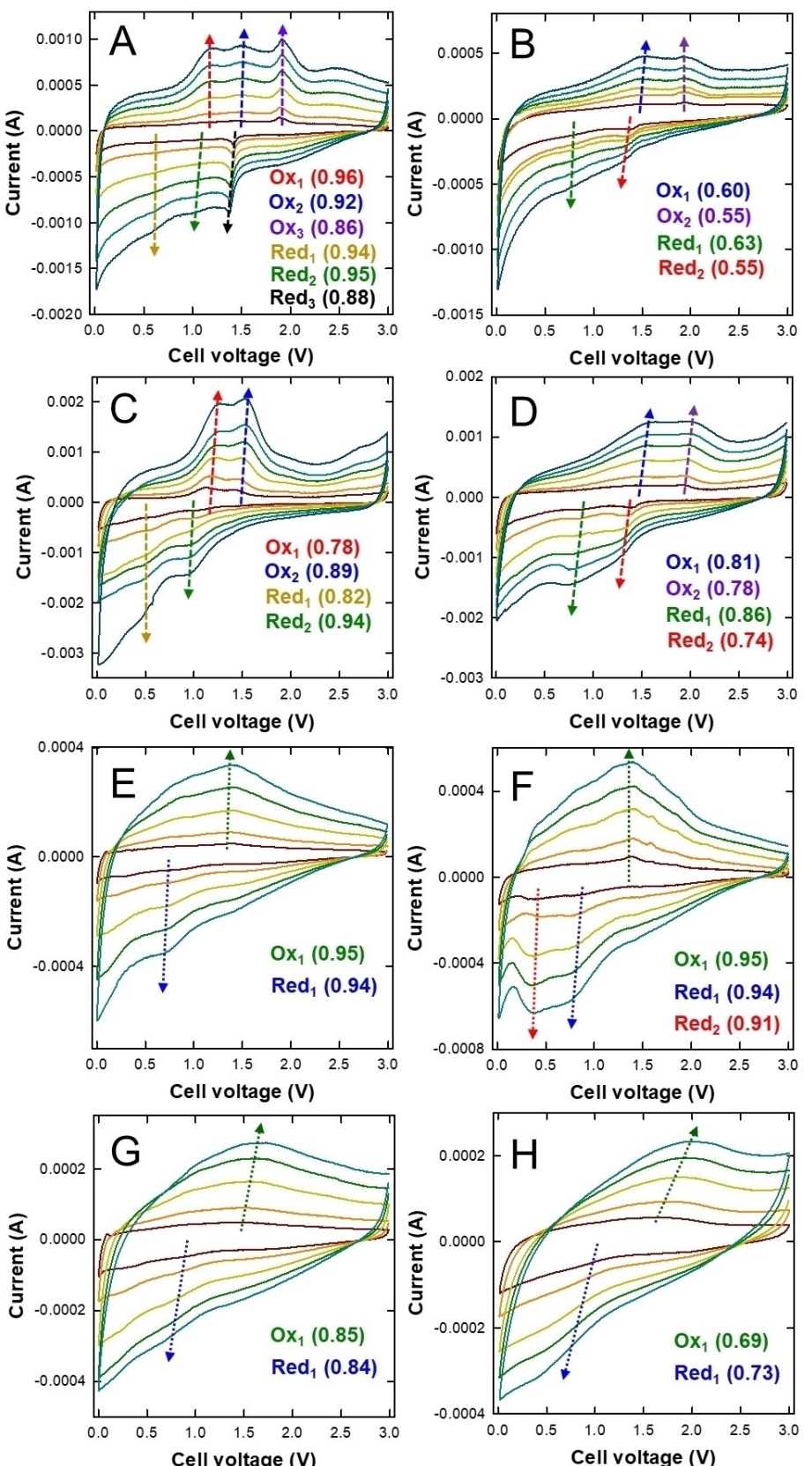


Figure 5. CV curves with 0.1–1.0 mV s⁻¹ for A and C) CNF1 and B and D) CNF2, A and B) before and C and D) after cycling toward LIB. CV curves with 0.1–0.8 mV s⁻¹ for E and G) CNF1 and F and H) CNF2, E and F) before and G and H) after cycling toward SIB. The CV curves colored with red, orange, yellow, green, cyan and blue were carried out under 0.1, 0.2, 0.4, 0.6, 0.8 and 1.0 mV s⁻¹, respectively. The value in round brackets indicates the *b*-values corresponding to the redox behavior.

ogy of the cycled cell is full of undefined small particles, which is observed for both hybrids (Figure S11). Especially, the severe capacity fading for the **CNF2** hybrid is attributed to the formation of the iron oxide phase during battery cycling, which degrades charge transfer kinetics. The transition from iron sulfide to iron oxide during SIB cycling might be due to the unstable $\text{Na}_y\text{Fe}_{1-x}\text{S}$ state formed during the conversion reaction. The observed better performance for **CNF1** with larger N-rich CN than **CNF2** highlights the beneficial effect of N-rich CN with the HI as a role of hybridization matrix or capacity generation.

CV measurements with different scan rates and an estimation of *b*-values based on the equation:

$$I = \alpha v^b$$

(*I*=measured current, *v*=sweep rate and *α*- and *b*-values=variable parameters), which allow us to understand an alteration in kinetic behavior for the redox couples for battery cycling.^[22] Given the *b*-values of **CNF1** before cycling is close to 1.0, the cycling performance of **CNF1** is mainly governed by (pseudo)capacitive behavior (Figures 5A and S12 A). Even after cycling that the Fe_{1-x}S is collapsed, the *b*-values related to a CN, or a HI still exhibit a high (pseudo)capacitive contribution (Figures 5C and S12 C). This is responsible for the constant battery performance without any degradation in spite of phase separation. For **CNF2**, unlike the initial behavior with a high contribution of the diffusion-controlled process, contribution of (pseudo)capacitive behavior significantly enhanced after 200 cycles (Figures 5D and S12D) and is responsible for the gradual growth of battery performance. For SIB, both **CNF** samples have *b*-values close to 1.0 with respect to the Fe_{1-x}S -derived conversion reaction, underscoring a large contribution of (pseudo)capacitive behavior on SIB performance (Figures 5E–5H and S12E–S12H). After battery cycling, however, the *b*-values of **CNF2** are markedly reduced which indicates a less contribution of (pseudo)capacitive behavior, ascribed to severe particle agglomerations or formation of iron oxide phase. This is starkly contrast to the **CNF1** which quite maintains its original *b*-values. Furthermore, a larger potential polarization in **CNF2** emphasizes slow electron transfer kinetics which is in good agreement with the aforementioned battery performance.^[23]

In conclusion, we have reported successful synthesis of N-rich CN– Fe_{1-x}S hybrids at 700 °C through in-situ chemical transition between Fe-incorporating MOF and a single precursor containing C, N and S atoms. According to TG-FTIR, we confirm significantly less N and S atoms being released upon hybridization, indicating the N and S atoms to be thermal-stabilized. Through a systematic investigation in electrochemical storage toward Li^+ and Na^+ ions, we suggest the beneficial effect of N-rich CN combined with a HI as a role of capacity contribution as well as a hybridization matrix. The **CNFs** prepared by current methodology appears to be quite active in LIB by delivering ~1750 mAhg⁻¹ at 0.1 Ag⁻¹ which is the highest value ever reported for iron sulfide-based hybrids. Even though the **CNF1** exhibits the specific surface area of <25 m²g⁻¹ (Figure S15), its SIB performance is higher than the other CN-based structure. We strongly believe that a facile

methodology introduced in this work for synthesizing N-rich CN-iron sulfide hybrids with a stable HI and their enhanced battery performance will offer a great potential for the design of new series of N-rich CN-based hybrids for energy storage and conversion applications.

Acknowledgements

A.V. acknowledges the University of Newcastle for the start-up grant for establishing the Global Innovative Center for Advanced Nanomaterials. X.Y. and M.B.H.B. would like to acknowledge the Singapore Synchrotron Light Source for providing the facility necessary for conducting the research. The Laboratory is a National Research Infrastructure under the National Research Foundation, Singapore. Any opinions, findings and conclusions or recommendations expressed in this material are those of the author(s) and do not reflect the views of National Research Foundation, Singapore.

Conflict of Interest

The authors declare no conflict of interest.

Data Availability Statement

The data that support the findings of this study are available from the corresponding author upon reasonable request.

Keywords: battery · C–N–Fe–S HI · hybrids · iron sulfide · N-rich carbon nitride

- [1] Y. Huang, B. Chen, J. Duan, F. Yang, T. Wang, Z. Wang, W. Yang, C. Hu, W. Luo, Y. Huang, *Angew. Chem.* **2020**, *59*, 3699–3704.
- [2] D. Masih, Y. Ma, S. Rohani, *Appl. Catal. B* **2017**, *206*, 556–588.
- [3] a) H. Yang, Z. Wang, S. Liu, Y. Shen, Y. Zhang, *Chin. Chem. Lett.* **2020**, *31*, 3047–3054; b) H. Yang, Q. Zhou, Z. Fang, W. Li, Y. Zheng, J. Ma, Z. Wang, L. Zhao, S. Liu, Y. Shen, Y. Zhang, *Chem.* **2021**, *7*, 2708–2721; c) S. N. Talapaneni, G. Singh, I. Y. Kim, K. AlBahily, A. H. Al-Mutaseeb, A. S. Karakoti, E. Tavakkoli, A. Vinu, *Adv. Mater.* **2019**, 1904635; d) G. P. Mane, S. N. Talapaneni, K. S. Lakhi, H. Ilbeygi, U. Ravon, K. Al-Bahily, T. Mori, D.-H. Park, A. Vinu, *Angew. Chem. Int. Ed.* **2017**, *56*, 8481–8485; *Angew. Chem.* **2017**, *129*, 8601–8605; e) K. S. Lakhi, D.-H. Park, K. Al-Bahily, W. Cha, B. Viswanathan, J.-H. Choy, A. Vinu, *Chem. Soc. Rev.* **2017**, *46*, 72–101; f) I. Y. Kim, S. Kim, S. Premkumar, J.-H. Yang, S. Umapathy, A. Vinu, *Small* **2019**, 1903572.
- [4] S. Kim, M. Hankel, W. Cha, G. Singh, J. M. Lee, I. Y. Kim, A. Vinu, *Nano Energy* **2020**, *72*, 104702.
- [5] H. Shang, Z. Zuo, L. Li, F. Wang, H. Liu, Y. Li, Y. Li, *Angew. Chem.* **2018**, *57*, 774–778.
- [6] I. Y. Kim, S. Kim, X. Jin, S. Premkumar, G. Chandra, N.-S. Lee, G. P. Mane, S.-J. Hwang, S. Umapathy, A. Vinu, *Angew. Chem.* **2018**, *57*, 17135–17140.
- [7] J. Li, H. Zhang, W. Samarakoon, W. Shan, D. A. Cullen, S. Karakalos, M. Chen, D. Gu, K. L. More, G. Wang, Z. Feng, Z. Wang, G. Wu, *Angew. Chem.* **2019**, *58*, 18971–18980.
- [8] M.-J. Choi, J. Kim, J.-K. Yoo, S. Yim, J. Jeon, Y. S. Jung, *Small* **2018**, *14*, 1702816.

- [9] S. N. Talapaneni, G. P. Mane, D.-H. Park, K. S. Lakhi, K. Ramadass, S. Joseph, W. M. Skinner, U. Ravon, K. Al-Bahily, A. Vinu, *J. Mater. Chem. A* **2017**, *5*, 18183–18192.
- [10] T. Marshall-Roth, N. J. Libretto, A. T. Wrobel, K. J. Anderton, M. L. Pegis, N. D. Ricke, T. V. Voorhis, J. T. Miller, Y. Surendranath, *Nat. Commun.* **2020**, *11*, 5283.
- [11] Y. Zhu, B. Zhang, X. Liu, D.-W. Wang, D. S. Su, *Angew. Chem.* **2014**, *53*, 10673–10677.
- [12] R. K. Hocking, E. C. Wasinger, F. M. F. de Groot, K. O. Hodgson, B. Hedman, E. I. Solomon, *J. Am. Chem. Soc.* **2006**, *128*, 10442–10451.
- [13] W. Cha, I. Y. Kim, J. M. Lee, S. Kim, K. Ramadass, K. Gopalakrishnan, S. Premkumar, S. Umapathy, A. Vinu, *ACS Appl. Mater. Interfaces* **2019**, *11*, 27192–27199.
- [14] J. Xu, J. Zhu, X. Yang, S. Cao, J. Yu, M. Shalom, M. Antonietti, *Adv. Mater.* **2016**, *28*, 6727–6733.
- [15] Q. Tang, Q. Jiang, T. Wu, T. Wu, Z. Ding, J. Wu, H. Yu, K. Huang, *ACS Appl. Mater. Interfaces* **2020**, *12*, 52888–52898.
- [16] a) F. Jiang, L. Zhang, W. Zhao, J. Zhou, P. Ge, L. Wang, Y. Yang, W. Sun, X. Chang, X. Ji, *ACS Sustainable Chem. Eng.* **2020**, *8*, 11783–11794; b) X. Zhang, X. Gao, J. Li, K. Hong, L. Wu, S. Xu, K. Zhang, C. Liu, Z. Rao, *J. Colloid Interface Sci.* **2020**, *579*, 699–706.
- [17] D. J. Parker, S. T. Chong, T. Hasell, *RSC Adv.* **2018**, *8*, 27892–27899.
- [18] D. Adekoya, X. Gu, M. Rudge, W. Wen, C. Lai, M. Hankel, S. Zhang, *Adv. Funct. Mater.* **2018**, *28*, 1803972.
- [19] Y. Liu, Y. Fang, Z. Zhao, C. Yuan, X. W. Lou, *Adv. Energy Mater.* **2019**, *9*, 1803052.
- [20] Y. Fu, Q. Wei, X. Wang, H. Shu, X. Yang, S. Sun, *J. Mater. Chem. A* **2015**, *3*, 13807–13818.
- [21] X. Jin, H. Huang, A. Wu, S. Gao, M. Lei, J. Zhao, X. Gao, G. Cao, *ACS Nano* **2018**, *12*, 8037–8047.
- [22] J. Wang, J. Polleux, J. Lim, B. Dunn, *J. Phys. Chem. C* **2007**, *111*, 14925–14931.
- [23] J. Liu, Y. Zhang, L. Zhang, F. Xie, A. Vasileff, S.-Z. Qiao, *Adv. Mater.* **2019**, *31*, 1901261.

Manuscript received: November 29, 2021

Revised manuscript received: December 18, 2021

Accepted manuscript online: December 24, 2021

Version of record online: January 12, 2022